AGU ADVANCING EARTH AND SPACE SCIENCE

Water Resources Research

RESEARCH ARTICLE
10.1029/2021WR030666

3D Flow Structures During Upwelling Events in Lakes of Moderate Size

Sergio A. Valbuena[1,2], Fabián A. Bombardelli[1,2], Alicia Cortés[1,2], John L. Largier[3,4], Derek C. Roberts[2,5], Alexander L. Forrest[1,2], and S. Geoffrey Schladow[1,2]

[1]Department of Civil and Environmental Engineering, University of California, Davis, CA, USA, [2]UC Davis Tahoe Environmental Research Center, Incline Village, NV, USA, [3]Department of Environmental Science and Policy, University of California, Davis, CA, USA, [4]UC Davis Coastal and Marine Sciences Institute, Bodega Bay, CA, USA, [5]San Francisco Estuary Institute, Richmond, CA, USA

Abstract Upwelling can impact water quality dynamics in stratified water bodies. Conceptual models generally classify the upwelling response to winds in lakes into either a non-rotational (2D, closed-basin) model or a rotational (coastal upwelling) counterpart. The non-rotational model is broadly applied in rotationally influenced lakes. The upwelling response to winds in stratified lakes may exhibit elements of both conceptual models. Here, we present the results of simulations with an accurate three-dimensional numerical model of a lake of moderate size (Lake Tahoe, California–Nevada, USA), and focus our analyses on addressing the influence of the Coriolis force during the upwelling setup and relaxation phases. Upwelling was observed at the upwind boundary as well as along the coast to the left of the mean wind direction due to Ekman-driven divergence. On the downwind shoreline, where downwelling occurs, alongshore currents appeared in response to wind forcing. Following the relaxation of the wind, our simulations reveal, for the first time, the existence of powerful cyclonic alongshore currents in lakes of moderate size, which are found to be in quasi-geostrophic balance. These currents followed the characteristics of coastal jets often observed in large lakes and the coastal ocean. Our work leads us to conclude that upwelling setup in lakes with length scales ≈20 *km* and Burger numbers $S < 1$, exhibits a combination of dynamics predicted by both the non-rotational, 2D, closed basin model, and the rotational coastal-upwelling conceptual model.

Key Points:

- Lakes of moderate size may exhibit upwelling at upwind shores and along-wind shores due to the Coriolis force influence
- Upwelling dynamics in lakes of moderate size cannot be parameterized by applying a single conceptual model
- Cyclonic currents observed in Lake Tahoe are in quasi-geostrophic balance and resemble coastal jets noticed in large lakes and coastal ocean

Supporting Information:

Supporting Information may be found in the online version of this article.

Correspondence to:

S. A. Valbuena,
savalbuena@ucdavis.edu

Citation:

Valbuena, S. A., Bombardelli, F. A., Cortés, A., Largier, J. L., Roberts, D. C., Forrest, A. L., & Schladow, S. G. (2022). 3D flow structures during upwelling events in lakes of moderate size. *Water Resources Research*, *58*, e2021WR030666. https://doi.org/10.1029/2021WR030666

Received 10 JUL 2021
Accepted 25 FEB 2022

Author Contributions:

Conceptualization: Sergio A. Valbuena, Fabián A. Bombardelli, John L. Largier, Derek C. Roberts, S. Geoffrey Schladow
Data curation: Sergio A. Valbuena, Derek C. Roberts
Formal analysis: Sergio A. Valbuena
Funding acquisition: S. Geoffrey Schladow
Investigation: Sergio A. Valbuena, Fabián A. Bombardelli
Methodology: Sergio A. Valbuena, Fabián A. Bombardelli, Alicia Cortés, John L. Largier, S. Geoffrey Schladow
Project Administration: Fabián A. Bombardelli, S. Geoffrey Schladow
Resources: Sergio A. Valbuena, Fabián A. Bombardelli, Alicia Cortés, John L. Largier, Derek C. Roberts, Alexander L. Forrest, S. Geoffrey Schladow

1. Introduction

During strong wind events over stratified lakes, the so-called dynamic equilibrium of the fluid becomes altered as energy is transferred from the air to the water layers (Imberger & Patterson, 1990; Kundu et al., 2015). In particular, the wind action may result in upward motions of deep, cold waters into the littoral zone as the lake-density structure responds to the surface wind stress—the well-known upwelling phenomenon. Upwelling of hypolimnetic waters provides a critical source of nutrients to the photic zone, increasing the pelagic productivity (Corman et al., 2010) and altering the ecological balance in the littoral zone (MacIntyre & Melack, 1995). The tilting of the thermocline promotes mixing, specifically in the littoral zone (MacIntyre & Jellison, 2001), along with littoral-pelagic mass exchange (Rao & Schwab, 2007). During relaxation, when upwelling winds weaken, complex phenomena characterize the nearshore area as internal waves may interact with lake morphometry, resulting in internal wave shoaling and breaking (Horn et al., 2001; Nakayama et al., 2020).

Two conceptual models are generally used to describe upwelling setup dynamics: *A non-rotational, two-dimensional (2D) upwelling model, and a rotational lake response to sustained wind events (coastal upwelling)*. In the latter model, Coriolis effects on the baroclinic response to wind events are often parameterized by analyzing the ratio of the internal wave celerity to the influence of the Coriolis force, that is, the Burger number, S (Antenucci & Imberger, 2001),

$$S = \frac{2c}{fL} = \frac{2L_r}{L}, \tag{1}$$

where c is the celerity of the fundamental internal-wave mode; f is the latitude-dependent Coriolis parameter; L is a flow length scale; and L_r is the Rossby radius of deformation.

Software: Sergio A. Valbuena, Alicia Cortés
Supervision: Fabián A. Bombardelli, John L. Largier, Alexander L. Forrest, S. Geoffrey Schladow
Validation: Sergio A. Valbuena, Fabián A. Bombardelli
Visualization: Sergio A. Valbuena
Writing – original draft: Sergio A. Valbuena, Fabián A. Bombardelli, Alicia Cortés, John L. Largier, Derek C. Roberts, S. Geoffrey Schladow
Writing – review & editing: Sergio A. Valbuena, Fabián A. Bombardelli, Alicia Cortés, John L. Largier, Derek C. Roberts, Alexander L. Forrest, S. Geoffrey Schladow

In large lakes, where $S \rightarrow 0$, such as the Laurentian Great Lakes, the upwelling response is formulated as in the coastal-upwelling conceptual model (Blanton, 1975; Csanady & Scott, 1974). This model predicts Ekman transport to the right of the wind in the northern hemisphere and upwelling along the boundary on the left side of the wind direction, where divergence in Ekman transport occurs. During severe wind events in large lakes, both periodic components such as Kelvin and Poincaré waves, and aperiodic components are excited. Aperiodic components may form the so-called "coastal jet" in basins wide enough that satisfy the criteria $fBc^{-1} \geq 1$ (Csanady, 1975), where B is the basin width perpendicular to wind stress. The coastal jet may thus be defined as the aperiodic response to alongshore winds, with width on the order of the internal Rossby radius of deformation (Csanady, 1982; Kundu et al., 2015). Following the theoretical approach by Csanady (1975), the coastal jet maximum velocity can be estimated as:

$$u_{\max} = \frac{1}{h_1} \int_0^t F_{baro} dt = \frac{Ft}{h_1}. \tag{2}$$

In Equation 2, h_1 is the surface-layer thickness; Ft is the time integrated surrogate of the wind stress; $F_{baro} = h_2\tau/(\rho_1 H)$ for the baroclinic mode where τ is the surface wind stress; H is the depth of the lake; h_2 is the thickness of the hypolimnion in a two-layer lake model; and ρ_1 is the density of the surface layer.

In turn, in lakes with $S \gg 1$, the 2D closed-basin upwelling model considers the lake response due to wind shear stresses to be constrained to the vertical plane of the mean wind direction. This conceptualization describes the upwelling setup as a steady-state linear tilt of the pycnocline parameterized by the Wedderburn number (W) (Thompson & Imberger, 1980):

$$W = R_i \frac{h_1}{L}, \tag{3}$$

where $R_i = g' h_1 / u_*^2$ is the bulk Richardson number; its inverse represents the linear slope of the pycnocline, and u_* is the shear stress velocity associated with the wind. W is usually applied to predict when upwelling occurs, but the parameterization is also often associated with the assumption of a non-rotational, 2D lake response during the upwelling setup (e.g., Roberts et al., 2021). Few studies have considered S along with W when analyzing upwelling events and addressing the occurrence of Kelvin and Poincaré waves after the relaxation of winds (e.g., de la Fuente et al., 2008; Stocker & Imberger, 2003). In many studies, the Wedderburn parameterization and the 2D model are used to identify and predict the spatial extent of upwelling, and to approximate the available potential energy during upwelling setup (e.g., Antenucci et al., 2000; MacIntyre et al., 2009). However, the influence of the Earth's rotation on the flow dynamics during the upwelling may generate a complex spatial pattern region and, by extension, water quality dynamics that differ from the predicted response when applying the non-rotational framework.

Different tools have been used to identify and understand upwelling events. For instance, researchers have used measurements of water temperature at the surface, and satellite imagery (e.g., Pöschke et al., 2015; Steissberg et al., 2005), whereas others undertook field deployments of temperature sensors and Acoustic Doppler Current Profilers, ADCPs (e.g., Blanton, 1975; Roberts et al., 2021). The field deployment of arrays of current, temperature, and water quality measurement devices on the upwelling-prone shore successfully captured upwelling dynamics (e.g., Csanady, 1972; Roberts et al., 2021). However, understanding of full-basin hydrodynamics during upwelling events using field data is inherently limited by the spatial coverage of instrument deployments. A comprehensive field study conducted in Lake Tahoe in 2018 (between May and July) captured the setup and relaxation dynamics of three large upwelling events of unusual magnitude (Roberts et al., 2021), where the setup was classified to follow the 2D non-rotational conceptual model and the relaxation was described as the combination of rotational and non-rotational flow structures. Despite the distinctive nature of the field deployment, important general questions remained unanswered due to limited spatial coverage (constrained to the prevailing upwind shore), such as the influence of Coriolis during the setup phase in the pelagic zone, and the nature of the observed alongshore currents.

Three-dimensional (3D) computer modeling can add understanding to the full-basin details of the lake dynamics as a complement to field studies. In particular, upwelling dynamics have been described by analyzing output from numerical models such as Si3D-L (e.g., Rueda, 2009), ELCOM or AEM3D (e.g., Valipour et al., 2019; Vidal et al., 2013), and MITgcm (e.g., Reiss et al., 2020). Motivated by a need to understand the Earth's rotation effects

on the flow structures generated during upwelling in lakes of moderate size (i.e., $S < 1$), historically characterized to follow the 2D, non-rotational model, we endeavored in this work to simulate such phenomenon by using the 3D hydrodynamic model PSi3D-L. This numerical model was previously validated and used satisfactorily in many lakes including Lake Tahoe, albeit with lower resolution. We use the events observed in Roberts et al. (2021) for calibration and validation purposes. We contribute to the understanding of the formation and nature of a coastal jet, and the role it plays in the littoral ecosystem. In addition, we provide insightful detail on the rotational effects on the flow structures that describe the complex lake response during upwelling and post-upwelling events in rotationally influenced lakes. We direct this work at addressing the following questions pertaining to lakes with stratification and length scales comparable to those observed in Lake Tahoe during the 2018 experiment (i.e., $L \approx 20{-}35\ km$ and $S < 1$):

1. Is the upwelling a fully rotational or non-rotational phenomenon?
2. Can upwelling dynamics be described by a single conceptual model?
3. What is the origin of the strong alongshore currents observed during the field deployment in 2018?
4. Do other factors affect the water quality during upwelling in addition to the upward flux of nutrients along the upwelling shore?

We first present the observations obtained in 2018 in Lake Tahoe and interpret the flow dynamics. In the following section, we describe the numerical model and results. We make a detailed analysis of the flow structures generated during upwelling and compare these with flow dynamics predicted by the non-rotational, 2D, and the rotational conceptual models. This work provides understanding of the Coriolis force effect during the upwelling setup, previously assumed to follow either one of the aforementioned conceptual models, and on flows observed during the relaxation stage. We then conclude with an analysis to address all factors that impact water quality during upwellings by applying a Lagrangian Particle Tracking (LPT) analysis.

2. Methods

2.1. Field Observations

Lake Tahoe, located at 1,897 m.a.s.l. in the Sierra Nevada Mountains (Figure 1a), is a deep, oligotrophic lake (maximum depth, 505 m; average depth, 313 m). Worldwide known for its clear waters (Secchi depth >20 m (Swift et al., 2006)), the lake has an annual mixing cycle where rapid convective cooling occurs during winter, followed by surface warming during spring and then deepening of the thermocline throughout the summer. Winds over Lake Tahoe are typically out of the southwest, displacing water in the surface boundary layer toward the northeastern shore and exhibiting upwelling, most commonly, on the west shore of the lake (Roberts et al., 2021; Schladow et al., 2004; Steissberg et al., 2005).

The field deployment in 2018 included a cross-shore transect on the west shore of the lake, thermistor chains on the south and eastern shores, and data from the existing long-term data collection framework at Lake Tahoe. The Homewood transect (HT) had a total of 6 moorings (A–F; Figure 1b) with current profilers, temperature, and pressure sensors (Table 1). The cross-lake south and cross-lake east (CLS and CLE, respectively) thermistor chains completed the deployment during the study period (May–July). While temperature and pressure were sampled every 30 s, velocity sampling period was 5 min with different bin spacing (Table 1). The Nearshore Network (NS) continuously collects data at 30 s interval, and the four buoys (TBx), managed by the National Aeronautics and Space Administration Jet Propulsion Laboratory, collect surface water temperature and atmospheric measurements at a 60 s period. For further details on the deployment at Lake Tahoe, we refer the reader to Roberts et al. (2021).

2.2. Numerical Model Implementation (PSi3D-L)

We used the parallelized version of the semi-implicit, 3D, free-surface hydrodynamic, numerical model for lakes (PSi3D-L), originally developed for estuarine circulation (see Smith, 2006) and extended for lakes by Rueda et al. (2003). PSi3D-L has been validated extensively, and used in Lake Tahoe and many other lakes with accurate results (e.g., Hoyer et al., 2015; Rueda et al., 2005, 2009). Detailed description of the numerical model is presented in Section S2 in Supporting Information S1, to which we refer to the interested reader.

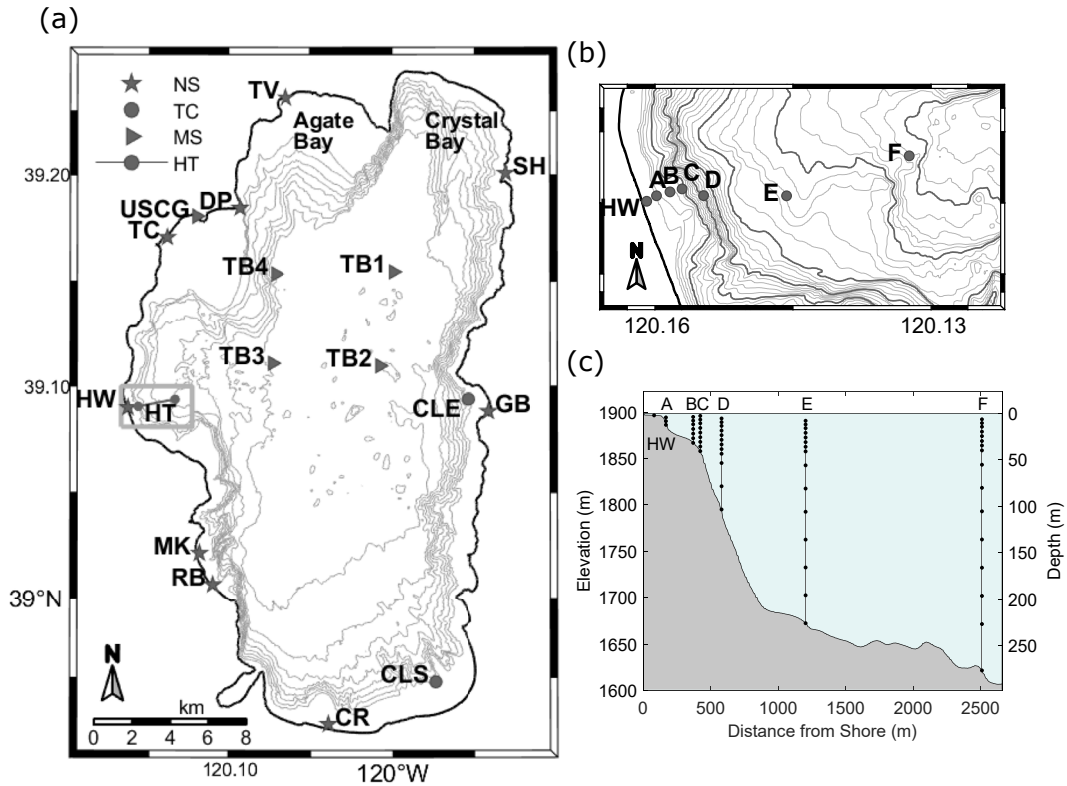

Figure 1. Plan and side views of the instruments deployed in Lake Tahoe with Nearshore Stations (*NS*), Thermistor chains (*TC*), meteorological stations (*MS*) and Homewood Transect (*HT*). (a) Location of sub-map (*HT*; gray box) and long-term data on a bathymetric map of Lake Tahoe with 50 *m* isobaths. (b) Detail of *HT* showing location of moorings described in Table 1. (c) Vertical plane along a West to East indicating transect from Homewood *HW* through F Vertical lines showing moorings with dots representing thermistor depths. Adapted from Roberts et al. (2021).

We simulated the 3D flow dynamics for three upwelling events captured during the field observation between 30 May 2018 and and 11 June 2018 (Roberts et al., 2021), using 5 days as model spin up time (i.e., simulations started on 24 May 2018 00:00). A $5-day$ period was considered enough based on previous simulations in lakes using the numerical model PSi3D-L, where 2 and 3 days were used as warm-up period (Rueda, 2009; Rueda & Schladow, 2003). Whereas the initial velocity field was specified as null, the temperature initial condition was established in the entire basin uniformly on the horizontal planes and vertically variable using a Sea Bird conductivity, temperature, and depth profile collected on 24 May 2018. Bathymetry of the lake was determined from existing 10×10 *m* bathymetric data. The grid size was chosen following mesh-independence test results, where horizontal velocity components were compared for diverse mesh sizes considered (200 *m*, 150 *m*, 100 *m*, and 75 *m*). Mesh-independence tests showed that velocity values did not have significant differences between grid sizes of 75 and 100 *m* (results not shown in here) and we finally adopted 100 *m*. Vertical resolution of the domain was chosen to properly represent wind-driven dynamics with 109 layers of variable thicknesses, where 0.5 *m* thick layers are at the surface and increase with depth reaching a maximum thickness of 13 *m* at 300 *m* of depth. Layer thicknesses for depths greater than 300 *m* decreased until reaching back 0.5 *m* thickness at the bottom of the lake (i.e., $H = 502$ *m*). In the simulations, the mesh was oriented in the directions $S-N$ and $W-E$ for y and x, respectively. The numerical simulations used a time step of 10 *s* to satisfy the Courant-Friedrichs-Lewy criteria for model stability and provided outputs with an interval set at 30 min. During the simulation time (20 *days*) lake level remained almost constant at 1,898.5 *m.a.s.l.* (*USGS 10337000 Lake Tahoe A Tahoe City CA*), and inflow/outflows volumes are negligible. While the vertical eddy viscosity and diffusivity were estimated using the 2.5 Mellor-Yamada hierarchy of turbulence closure models (Kantha & Clayson, 1994), we used the Smagorisnky type model for the horizontal mixing coefficients. These methods provided the best results during the calibration period.

Table 1
Summary of 2018 Field Deployment and Existing Long Term Data Collection Framework in Lake Tahoe

Project sites	Depth (m)	Thermistors (m)[a]	ADCP	
			Bin Step	Depth range (m)
A	11.3	0, 4, 8	0.25 m	0.3–6.6
B	31.0	0, 5, 10, 15, 20, 24, 28	0.5 m	0.6–27.6
C	41.5	0, 5, 10, 15, 20, 25, 30, 34, 38	0.5 m	0.6–36.6
D	106.6	0, 25, 50, 60, 65, 70, 75, 80, 85, 90, 94, 98	1 m	11–110
E	225.4	0, 30, 60, 90, 120, 145, 170, 185, 190, 195, 200, 205, 210, 214, 218	2 m	7–151
F	277.4	0, 50, 80, 110, 141, 171, 197, 222, 237, 242, 247, 252, 257, 262, 266, 270	–	
CLE	64.7	0, 25, 30, 35, 40, 45, 50, 58	–	
CLS	62.5	0, 25, 30, 35, 40, 45, 50, 58	–	

Existing sites	Station type	Instruments/Measurements	Sampling period
NS	WQ	Temperature, conductivity, pressure, turbidity, Chl-a, and CDOM	30 s
USCG	MET	Air temp, wind speed/direction, relative humidity, air pressure, shortwave and longwave radiation (incoming and outgoing)	10 min
TB1-TB4	MET & TEMP	Air temp, wind speed/direction, relative humidity, air pressure, and water temperature at 0.5 m, 1 m, 1.5 m, 2 m, 4 m, 5 m, and 5.5 m	1 min

Note. Data used for model calibration and validation, and meteorological forcing in the numerical model. CLE, cross-lake east; CLS, cross-lake south. MET, Meteorological station; NS, Nearshore Network at 2 m deep; TEMP, Temperature measurements; WQ, Water Quality at 2 m deep.

[a]Thermistors (m), Meters above bottom; Thermistors used sampling period = 30 s.

The surface boundary condition applied meteorological data available for the same period. In 2018 between May and July, *USCG* and $TB1-4$ (Figure 1a and Table 1) were the only stations providing meteorological data and thus, uniform surface values were assumed. Strong wind fronts generate quasi-uniform wind fields over the surface of the lake (Roberts et al., 2019), and this justifies the use of a spatially uniform surface boundary condition (see also Reardon et al., 2014). Data from $TB1-4$ were interpolated to match the frequency of records for the solar radiation parameters and used as the forcing inputs. Air temperature, wind speed/direction, relative humidity, and barotropic pressure records were collected from the four buoys, and shortwave and longwave radiation inputs were obtained using the Lake Tahoe United States Coast Guard station (*USCG* on Figure 1a).The model used a time variable attenuation coefficient of light penetration from weekly Secchi depth measurements and implemented via the surface boundary condition. The relationship between Secchi depth and the attenuation coefficient was estimated following Martin and McCutcheon (1999). Description of data used as surface boundary conditions is shown in Figure S2 in Supporting Information S1.

2.3. Upwelling Timing in the Lake Tahoe Model

The timing of upwelling events is determined by analyzing when the surface temperatures drop due to the pycnocline breaking the surface (Thompson & Imberger, 1980). Thus, the temperature of the thermocline is used as a threshold value to identify the start and end of the upwelling event. The basin-wide maximum vertical density gradient from the numerical results was used to estimate the temperature and depth of the thermocline as follows: $10.2°C$ and $12.2\ m$ for the first upwelling event, and $10.2°C$ and $15\ m$ for the third upwelling; these results are in agreement with those in Roberts et al. (2021): $14.95\ m$ and $10.1°C$. Tracking the thermocline allowed to determine that the first and third upwelling events break the surface on 30 May 2018 15:00 and 9 June 2018 04:00, and end on 8 June 2018 21:00 and 20 November 2018:00, respectively (from now on E1 and E3).

We focus our analysis on describing the lake response during the events that started on 30 May 2018 and 8 June 2018. The second event, on 05 June 2018, forced by two wind pulses (6 *hr* on 4 June 2018 and 8 *hr* on 5 June 2018), was the weakest upwelling event during the study period and exhibited a complex response not well resolved by the numerical model.

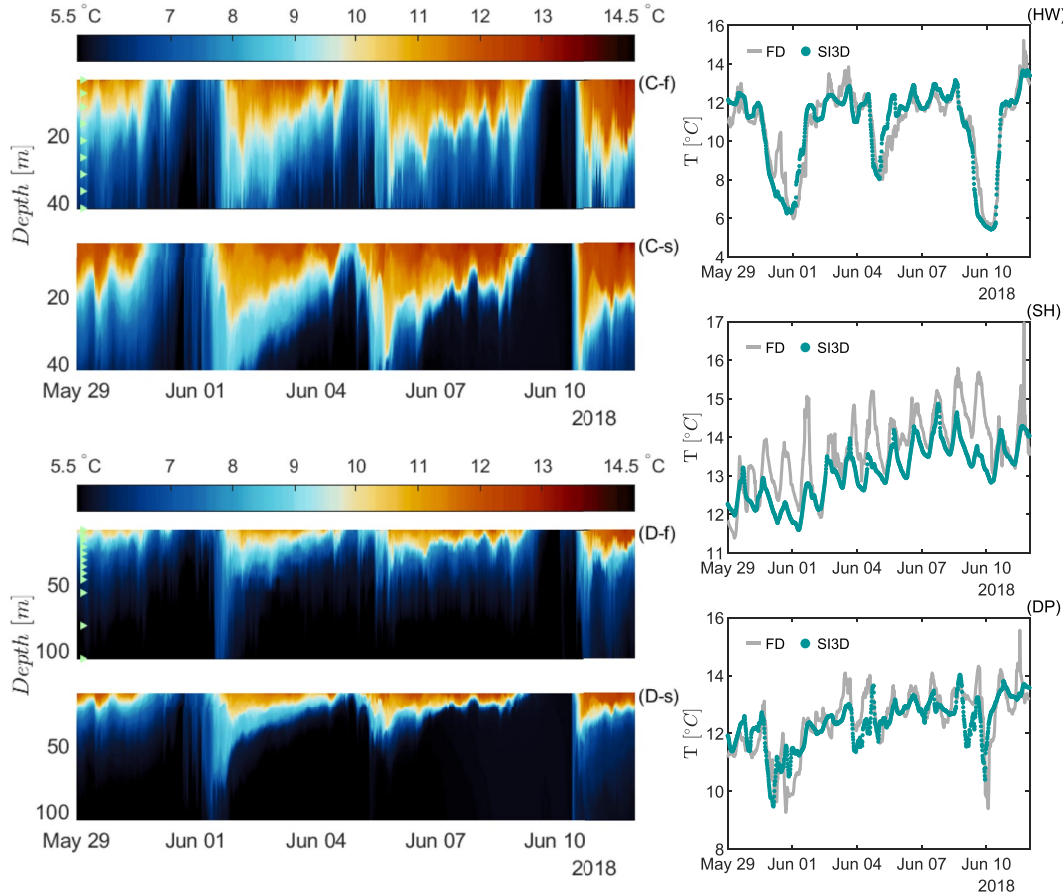

Figure 2. Calibration and validation of the numerical results regarding temperature; tile names indicate the site location from Figure 1. Time series plots are named by site followed by *-f* or *-s* for field and PSI3D-L results, respectively. Legends refer to field data (FD) and PSI3D-L results (SI3D). Light green triangles on -f represent the depth of each thermistor used in the validation. In line plots we show temperature time series at ≈2 *m* of depth.

3. Results

3.1. Model Calibration and Validation

Initially, we verified the hydrodynamic model by using a hypothetical wind driven test case (see Section S3 in Supporting Information S1). Calibration of the hydrodynamic model was undertaken by modifying the bottom drag coefficient and we corroborated that the best model performance for a simulated period that considered only E1. A bottom drag coefficient of 0.004 provided the best prediction of flow and temperature fields at sites with shallow water levels and it was used for the validation of the numerical model.

The calibrated set up at E1 was then used to simulate the entire period. Time series of simulated (-s, SI3D) and observed (-f, FD) temperatures at sites C, D, HW, SH and DP are compared in Figure 2. Line plots represent the comparison at nearshore stations located at ≈2 *m* of depth. Other comparisons in other locations are presented in Figures S3–S7 in Supporting Information S1. In Figure 2-([C-f, C-s]) and ([D-f, D-s]), good agreement is observed both in time and space (depth). Upwelling events that started on 30 May 2018 and 08 June 2018 were forced by sustained winds that formed an uniform wind front over the water's surface. During these events, upwelling-driven lake dynamics were correctly predicted by the model (Figure 2). The upwelling event between 4–5 June 2018 resulted in an absolute error of up to 2°*C* during the second wind pulse, which is the maximum error found during the entire simulation period. The two wind pulses of variable wind speed and direction observed during E2 were not of sufficient duration to create an uniform wind field on the lake's surface, justifying the differences between simulated and observed temperatures during this event.

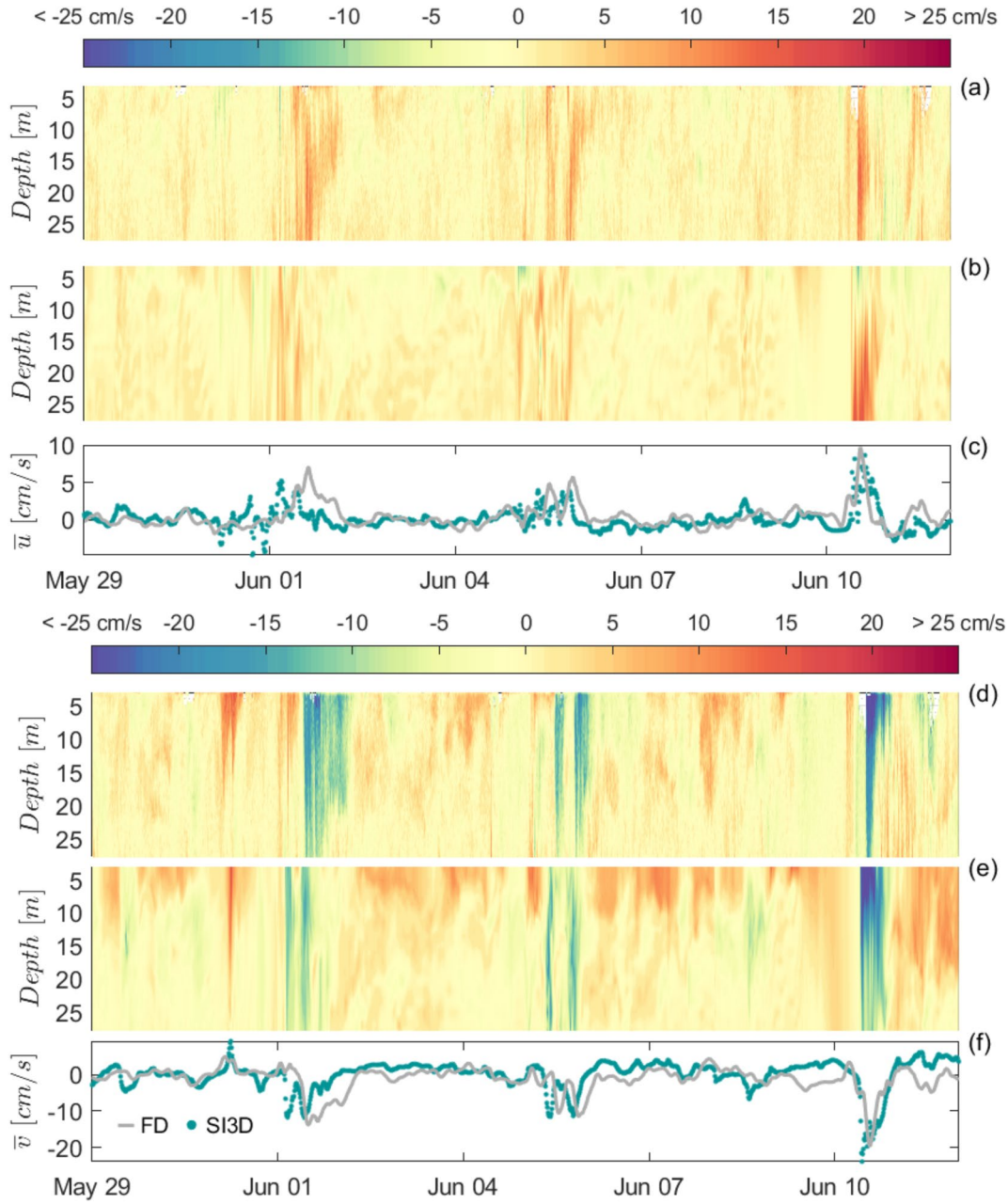

Figure 3. Calibration and validation of numerical results of horizontal velocity components for site B. Top plots (a, d) are field records for the *u* and *v* components respectively; (b, e) are the PSI3D-L results for *u* and *v* components; (c, f) are the depth-averaged velocity for the corresponding component. Peak velocities were up to 0.35 ms^{-1} for both horizontal components.

Good agreement of predicted velocities during the entire simulation period, and accurate prediction of magnitude and direction of the along-shore and off-shore currents during upwelling and relaxation is evident at site *B* (Figure 3) and at other sites in the Homewood Transect (Figures S8–S11 in Supporting Information S1).

Numerical results were also validated using temperature and velocity data collected at stations A to CLS (Table 1), and temperature records from the Nearshore Network stations HW, TC, TV, SH, and DP. For proper computation of the model-performance metrics, field measurements were re-sampled at 15 min intervals and numerical results were interpolated to match depth of observations. We verified the agreement between measured and simulated water temperatures by estimating the Model Skill Score (SS) (Murphy & Epstein, 1989), error norms

Table 2
Statistical Metrics for Model Performance Validation

Stat	A	B	C	D	E	F	HW	TC	TV	SH	DP	CLS	CLE
Temperature													
SS	0.802	0.773	0.811	0.836	0.895	0.865	0.865	0.776	0.473	0.401	0.513	0.683	0.806
I1	0.0634	0.078	0.079	0.069	0.058	0.065	0.057	0.054	0.042	0.054	0.046	0.113	0.085
I2	0.088	0.109	0.106	0.099	0.085	0.099	0.76	0.068	0.053	0.065	0.059	0.161	0.134
RMSE (°C)	0.896	1.011	0.902	0.741	0.603	0.696	0.829	0.837	0.692	0.894	0.743	1.437	1.159
Velocity													
RMSE (m/s)	0.047	0.037	0.032	0.031	0.063					–			
$RMSE_u$ (m/s)	0.032	0.031	0.031	0.034	0.052					–			
$RMSE_v$ (m/s)	0.063	0.045	0.078	0.037	0.054					–			
$RMSE_w$ (m/s)	0.003	0.004	0.004	0.008	0.017					–			

Note. RMSE for the velocity magnitude. Error per velocity component and TB1-4 metrics results are shown in Supporting Information S1. RMSE, Root Mean Square Error.

I_1 and I_2, and Root Mean Square Error (*RMSE*) according to definitions included in Section S4 in Supporting Information S1.

Table 2 presents the results of the statistical metrics. The performance metric estimations included all days of the simulation (29 May 2018–12 June 2018). Following Scheu et al. (2018), the results for SS show excellent (0.65–1) and very good (0.5–0.65) agreement on most of the sites, with the highest error at the locations with greater depth (i.e., E and F). The norms I_1 and I_2 were on average 0.068 and 0.158 for the whole lake and are comparable with results available in the literature ($I_1 \leq 0.125$ and $I_2 \leq 0.164$; Rueda & Schladow, 2003; Hodges et al., 2000). *RMSE* values show that differences are greater on the shallowest sites (*A* and *B*) and at southeastern and eastern sites CLS and CLE, respectively. The maximum error was $1.437°C$, value of the same order of magnitude as recent 3D hydrodynamic model results in Lake Erie, where *RMSE* of up to $1.5°C$ was obtained (see ESM Valipour et al., 2019).

When comparing the simulated and measured velocities at sites A, B, C, D, and E, we used the *RMSE*, estimated to be between 0.003 ms^{-1} and 0.061 ms^{-1} for the velocity components u, v, and w (Table 2). Field observations recorded peak velocities exceeding 0.25 ms^{-1} for the horizontal components u and v, and exceeding 0.02 ms^{-1} for the vertical component w (see Figure 6 in Roberts et al., 2021). Agreement of simulated velocity to field measurements is overall good, with maximum *RMSE* of 0.049 ms^{-1}, 0.061 ms^{-1}, and 0.017 ms^{-1} for u, v, and w, respectively. Similar levels of agreement have been found in previous 3D modeling studies. For instance, Scheu et al. (2018) reported errors from 0.05 ms^{-1} up to 0.18 ms^{-1} for peak velocities around 0.3 ms^{-1}, and Valipour et al. (2019) reported *RMSE* of 0.076 ms^{-1} and 0.072 ms^{-1} for the u and v components respectively with velocities between 0.1 ms^{-1} and 0.3 ms^{-1}. Therefore, we conclude that the numerical model adequately represents the 3D velocity field during the simulation period, when complex flow patterns due to upwelling events were present.

To our knowledge, upwelling events of extreme magnitudes as the ones observed at Lake Tahoe in 2018 have not been reported before Roberts et al. (2021). The good agreement between the field data and numerical results exhibits the capability of the numerical model to properly predict lake hydrodynamics under severe winds.

3.2. Upwelling Dynamics

The lake response to winds exhibited the same dynamics in each event, and differences between upwelling events were limited to the magnitude of excursions of isotherms, extent of upwelled area, and thermocline deepening on the northeast and eastern shores. In Figures 4a–4d and 5a–5d we show the setup stage for each upwelling event, where velocity vectors indicate the depth-averaged velocity in the relative Ekman layer. We defined the Ekman depth as the minimum of the pycnocline depth (≈15–55 m) or the relative Ekman depth $E_z = \sqrt{2\nu_v/f} \approx 45\ m$, where $\nu_v \approx 0.1\ m^2s^{-1}$ was estimated from the numerical simulations as the mean vertical eddy viscosity in the surface layer.

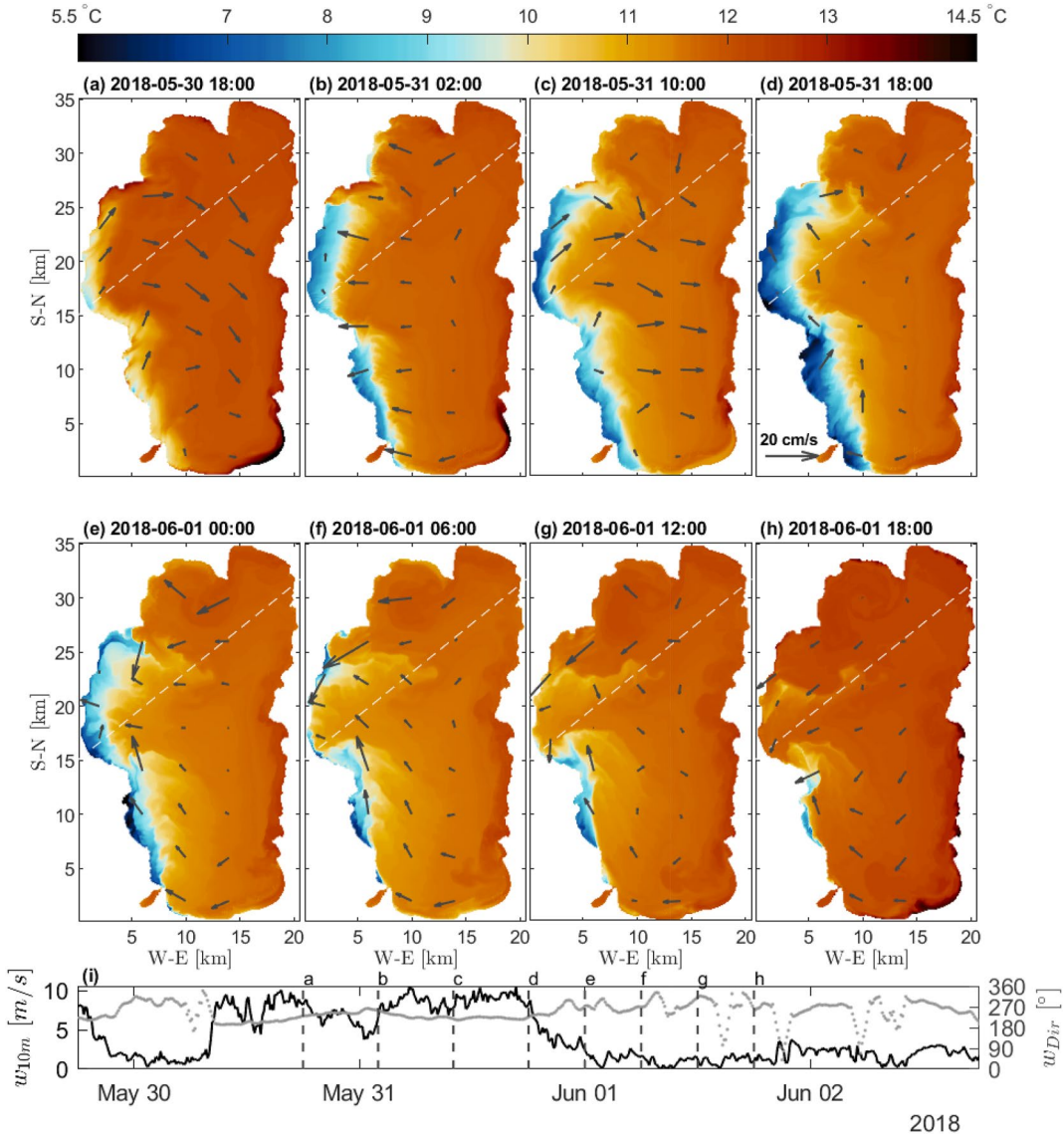

Figure 4. Evolution of surface temperature during E1 as snapshots with Ekman depth-averaged velocity vectors (gray) and mean wind direction (white dashed line from left to right) during upwelling setup (a–d) and upwelling relaxation (e–h). Panel (i) shows the wind speed (black) and direction (gray) time series during upwelling event.

Wind forcing during E1 reduced on the night of 30 May 2018 allowing restoring baroclinic forces to drive warm surface water toward the west shore (Figure 4b) before a second wind pulse continued the event. During E1, downwelling was observed on the northeast and eastern shores of up to 35 m, and surface temperatures dropped $\approx 5°C$ on the western shores (Figure 4d). In contrast to E1, wind forcing during E3 formed a single event with wind speeds up to 16 ms^{-1} (see Figure 5) generating an upwelled region of approximately half of the lake's surface area (10 km from west shore). This strong forcing upwelled isotherms as much as 70 m and temperatures decreased as much as $7°C$.

During upwelling setup, upward motions of 0.5–1.2 cms^{-1} are observed. As wind forcing continued, off-shore currents (northeastward and eastward currents) generated a thermal front non-perpendicular to the mean wind direction (mean southwestern winds with 230° and 210° for E1 (Figure 4) and E3 (Figure 5), respectively). Although the boundaries limit Ekman dynamics, Ekman transport developed in the pelagic zone and rotational effects increased with the passing of time. Rotational effects resulted in upwelling along boundaries to the left of

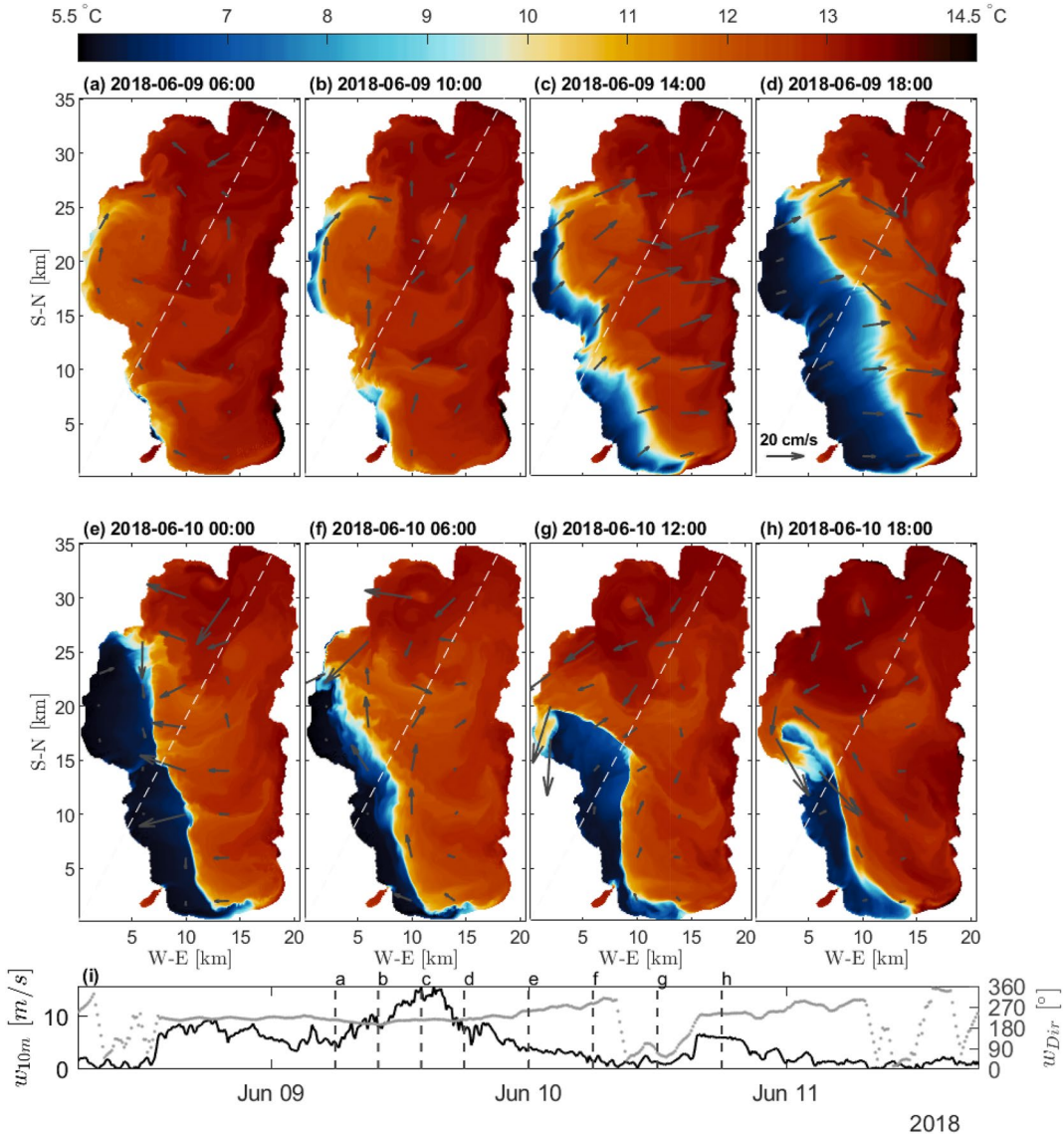

Figure 5. Evolution of surface temperatures (colormap) during upwelling event E3. Same description as for E1.

the wind direction (See blue-like colors in Figures 4c, 4d, 5c, and 5d), with surface cooling at the northwestern shore site Dollar Point (i.e., DP in Figure 1) during E1 and E3 (Figure 2 [DP]).

During upwelling setup, surface currents near the upwind shore were quasi-parallel to the wind direction. At distances $\geq$6 *km* from this shore, surface currents were deflected to the right of the wind direction during both upwelling events due to rotational effects (Figures 4a–4c and 5c–5d). This Ekman response was seen throughout the surface mixed-layer and yielded an increased surface elevation at the northeastern and eastern shores (from now on the downwelled region). Simultaneous with the thermocline tilting, northward alongshore currents formed along the eastern shores with jet-like structure and maximum velocities of 20 cms^{-1} and 35 cms^{-1} for E1 and E3, respectively (Figures 6a–6c and 7a–7c).

In Figures 6 and 7, a 3D view of the aforementioned flow structures observed during upwelling setup is presented. In the figures we show the coastal jet flow structure in the forefront plane as filled contours with negative values for velocities with direction out of the plane (southern currents). In the other planes, we indicate positive values for flows with eastern direction (to the right of the figure). The water temperatures and velocity contours represent the 3D rotational flow structures observed during the relaxation phase. In the absence of wind, restoring

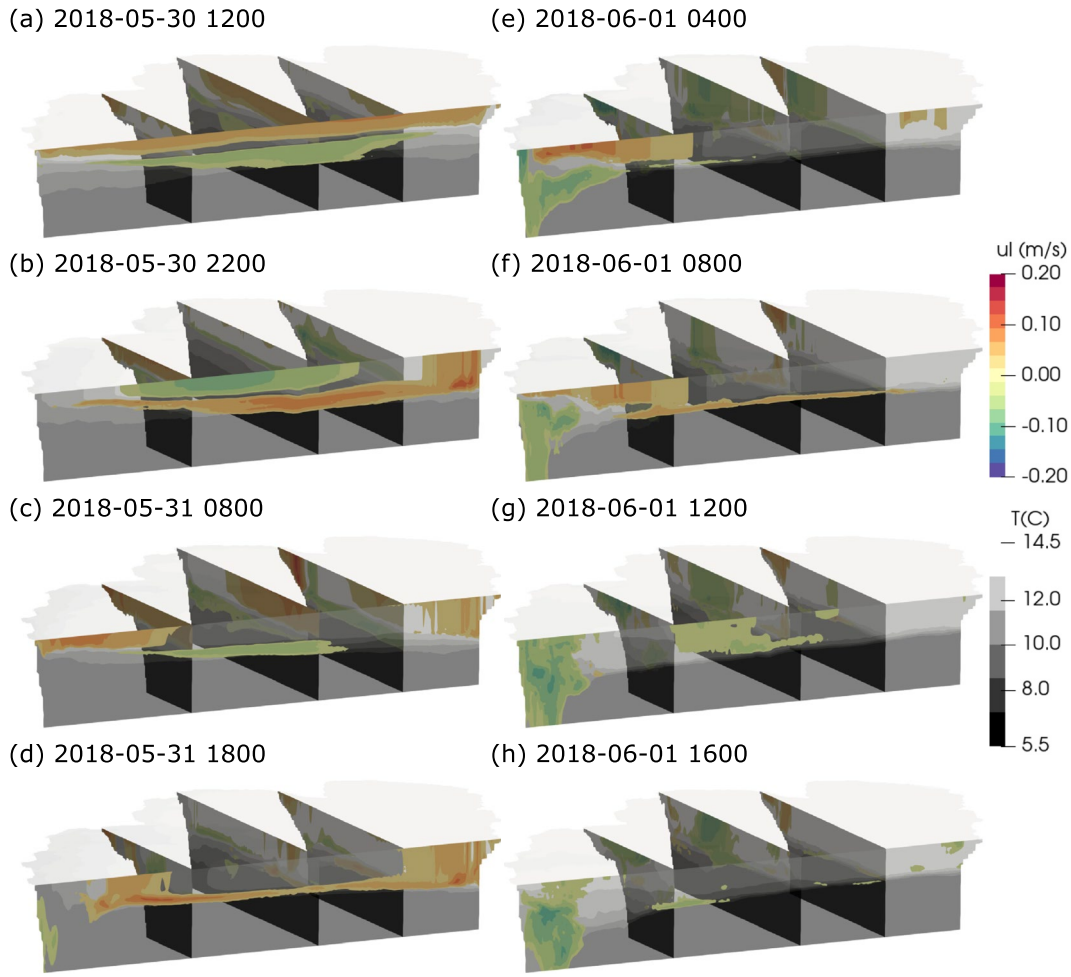

Figure 6. Top 60 *m* evolution of currents and temperature profiles for E1 during wind forcing (a–d) and upwelling relaxation phase (e–h) on the northern part of Lake Tahoe represented as vertical planes. Plane located in the forefront is perpendicular to the mean thermal front angle (110°) with Homewood Nearshore Station (*HW* Figure 1) as initial position on the west shore. In each plane, colors indicate temperature ($°C$). Superimposed to the surface colors, filled contours refer to plane-normal velocities (ms^{-1}) colored by its magnitude.

forces from the horizontal density gradients forced the warm surface layer to move toward the upwelled shore (Figures 4e–4f and 5e–5f). As the warm front moved west, it became deflected to the north with the cold surface currents being rotated toward south. As the thermal front progressed westward, vertical length scales of up to 100 and 70 *m* developed for E1 and E3, respectively. Time series of vertical profiles of field and simulated temperature exhibit the thermal front and the vertical extent of this relaxation flow (Figure 2 [D-f, D-s]).

The pelagic zone the return flow is influenced by rotation and becomes parallel to the thermal front, forming a quasi-geostrophic front that propagates slowly. This slowed down the return of the warm surface layer to the upwelled shore following both upwelling events, as shown by the positive velocities on the frontal plane in Figures 6 and 7. This phenomenon can also be observed by comparing the fast progress of the sharp thermal front between snapshots (e) and (f) ≈ 3 *km* and the slow progress of the surface density interface from snapshots (f)–(h) in Figure 5 (≤ 1 *km*). During the westward relaxation of the warm front, convergent surface flows produce vertical velocities of up to 1.6 cms^{-1} for E1 and E3, and horizontal currents of up 15 cms^{-1} (E1) and 35 cms^{-1} (E3) were observed in the numerical results. Strong surface convergence occurs when this flow structure contacts the west shore and isotherms are observed to downwell to 50 *m*, rewarming the west shore and remaining highly active afterward.

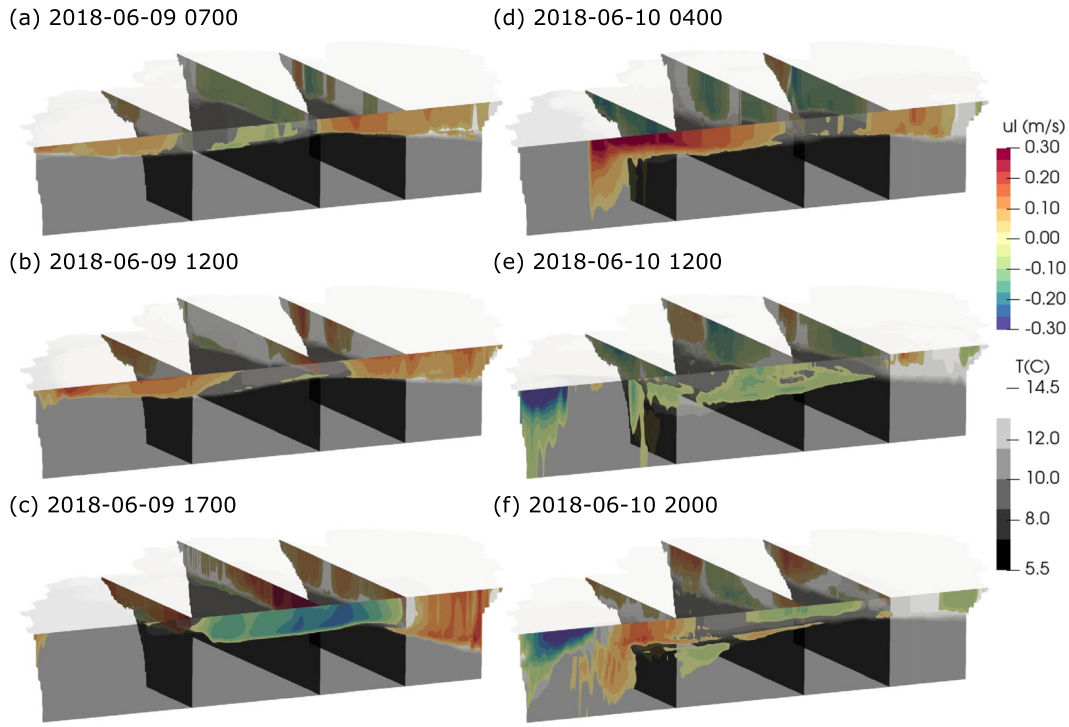

Figure 7. Evolution of currents and temperature profiles for E3 during wind forcing (a–c) and upwelling relaxation phase (d–f). The figure follows the same description as in Figure 6.

While northward currents developed along the downwelling shore during active wind forcing, due to shore-normal water-level gradients and thermocline tilt, this strong shore-parallel flow persisted after wind forcing weakened (i.e., during relaxation phase). This counterclockwise flow resembles a coastal jet (see below Section 4). Trapped to the shore, this rotational flow structure progressed simultaneously with the westward migration of the thermal front across the center of the lake with velocities similar to those observed in the warm surface layer. Average velocities of 15 cms^{-1} and 20 cms^{-1}, during E1 and E3, respectively, characterize the jet traveling along the shore. This shore-attached flow arrived at the west shore at the same time as the whole-lake relaxation front during E1 and before the front during E3. This can be seen in Figures 4g and 5f–5h, where the surface temperature details the cyclonic currents on the northwestern and western shores. In addition, we show in Figures 6 and 7 the counterclockwise motion of the jet flowing along the northern and western shores after the wind dies.

The alongshore currents arrived at Homewood (*HW* in Figure 1) approximately between 17 and 19 *hr* (for E1 and E3, respectively) after upwelling relaxation phase initiated with a consistent extent between 2 and 3.5 *km* from the shore during upwelling setup (east shore) and upwelling relaxation (north and west shores). Following the passage of the flow structure, offshore currents increased the extent while dissipating this flow structure.

3.3. Time Evolution of Thermocline

Evidenced by the surface elevation rise and consequent tilting of the thermocline, barotropic pressure gradients evolved as wind stress pushed surface waters toward the downwelled shore. Combination of surface cooling along the upwind boundary and along the boundary to the left of the wind direction, characteristic of both non-rotational and rotational conceptual models, describe the lake response during wind forcing (Figures 5c–5d and 8a–8c). During the setup phase, with southwestern mean wind direction, the upwelling was observed on the south (*CR*), west (*RB*, *MK*, *HW*, and *TC*), and northwestern (*DP*) shores (Figures 2, 4, and 5).

In contrast to a linear tilt of pycnocline orthogonal to the wind direction, expected from the non-rotational conceptual model, numerical results showed thermocline deepening on the eastern shores of the lake as well as along the downwind shore. During upwelling events, Ekman transport in the surface layer promoted downwelling on the eastern shore (Figure 8). The mean wind direction during E3 (210°) may contribute to the increase in the

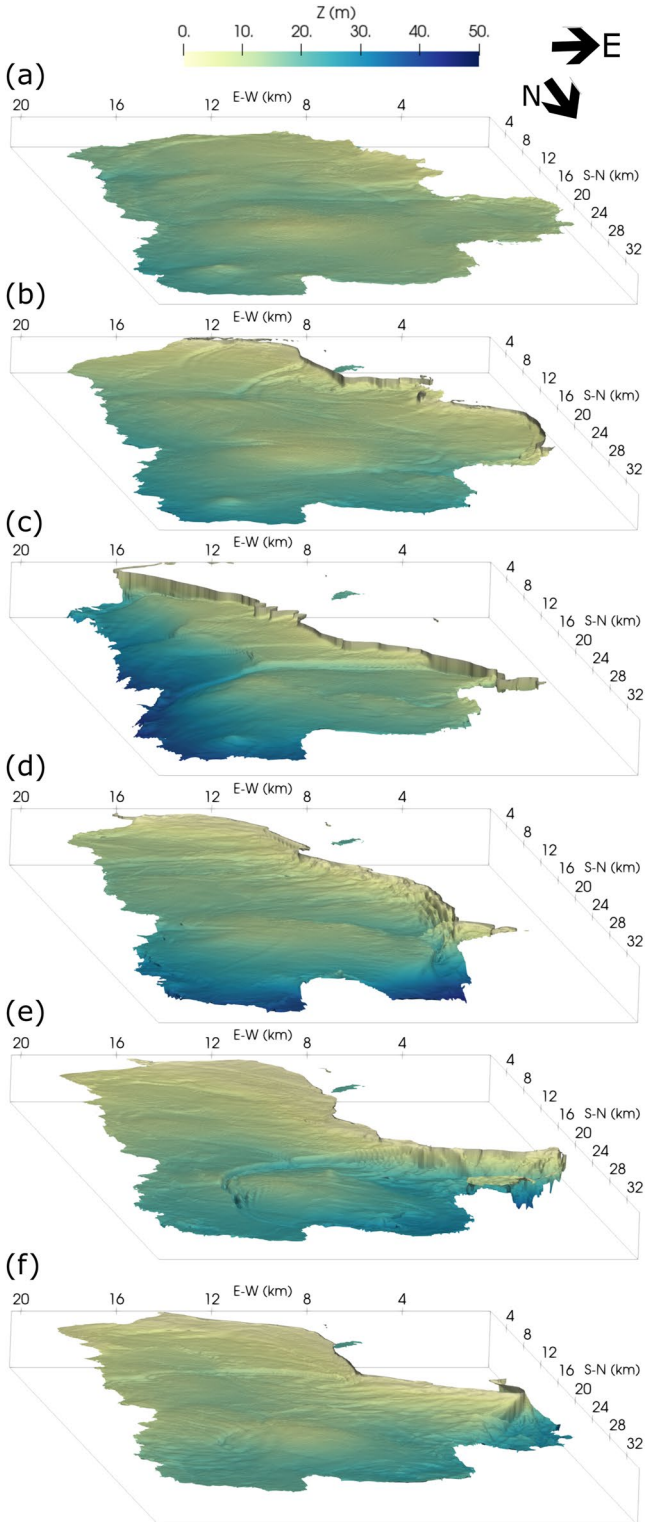

Figure 8. Snapshots of the thermocline during upwelling setup and relaxation phases for E3 (i.e., 10.2°*C* thermocline isosurface). Pycnocline colored by the depth at: (a) surface excursion, 8 June 2018 21:00:00; (b) upwelling setup, 9 June 2018 12:00:00; (c) peak of thermocline tilt, 9 June 2018 17:00:00; (d–f) relaxation phase with alongshore currents on north and western shores.

surface elevation and downwelling expressions on the east shore. Although, the limited wind fetch (≈3–8 *km*) on the southern portion of the lake unlikely contribute significantly to the increase on the surface elevation on the eastern shore.

3.4. Particle Motions

Using the results coming from the PSi3D-L, and a LPT Tool built in *ParaView 5.9.1*, we addressed particle motions in the upwelled region and the potential of the coastal jet signal as a water quality driver during upwellings. The LPT solves for the 3D transport of massless particles (i.e., particles that move along with the velocity field). We focused only on the third upwelling event E3 as the flow structures are more well-defined due to stronger wind forcing. Particles were released at the beginning of E3 (i.e., 8 June 2018 18:00:00), at about 1,500 *m* away from the shores on the upwelled and downwelled coasts. Distributed in a spherical shape, a total of 100 particles were released at multiple depths ranging between 0 and 40 *m*.

During upwelling setup, the particles developed an upward trajectory and horizontal offshore transport on the upwelled shore (west), and northward trajectories on the downwelled shore (northeast and east). After wind relaxation, particles on the downwelled shore described counterclockwise alongshore motions, represented as the transition from red to white color. Particles on the upwelled shore (west shore) exemplify the upward flux of constituents, later followed by horizontal offshore transport of the top layers during wind forcing (Figure 9). After the intensity of wind reduces, return flow of the warm surface layer caused downward motions that drive particles to depths below 60 *m*.

Furthermore, particles released on the east shore reached deeper waters as downwelling increased. Northern alongshore transport of the particles due to coastal jet currents is evident at snapshots (a) and (b) of Figure 9 (i.e., during upwelling setup). Particles released on the east shore experienced a maximum westward excursion of up to 17 *km* along the shore after wind relaxation, implying a relevant role of the coastal jet as a water quality driver. The advection of particles appear to be trapped along the northern shore and exhibited bathymetric effects.

4. Discussion

4.1. Rotational Effects on Upwelling Setup

As mentioned before, the lake's response to wind forcing is a combination of upwelling at the upwind boundary and along the boundary to the left of the wind direction. While the non-rotational conceptual model can account for the observed surface cooling on the south and western shores, upwelling observed along the northwestern shore (*DP*) is not consistent with this conceptual approach (Figure 2-[*DP*]). To better understand rotational effects we performed numerical simulations excluding the Coriolis term in the momentum equations. Such results show surface cooling along upwind boundaries but not at *DP*, or along the northwestern shore, which is a downwind boundary (Figures 10a and 10b). Comparison of the simulations with and without Coriolis force imply that upwelling observed at *DP* can only be explained by rotational effects that results in Ekman-driven divergence along northerly coasts and a thermal surface front that is not orthogonal to wind direction.

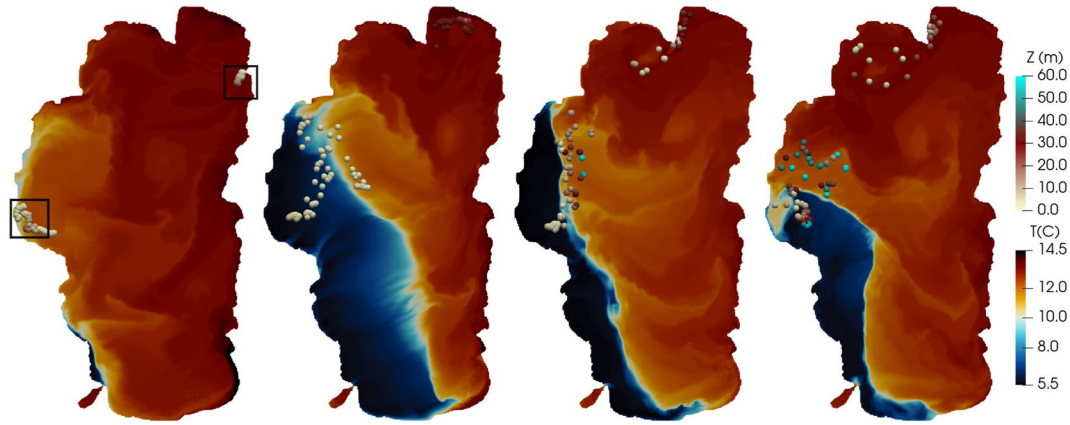

Figure 9. Snapshots from release of particles on the west and east shores of Lake Tahoe. The snapshots are at: (a) Surface excursion, 13 *hr* after particle release; (b) Upwelling setup, 25 *hr*; (c) Upwelling relaxation, 34 *hr*; and (d) Alongshore currents on western shores, 43 *hr* after E3 initiated, time of particles release. Z indicates the depth of the position of the particles and black squares show the release area at each shore.

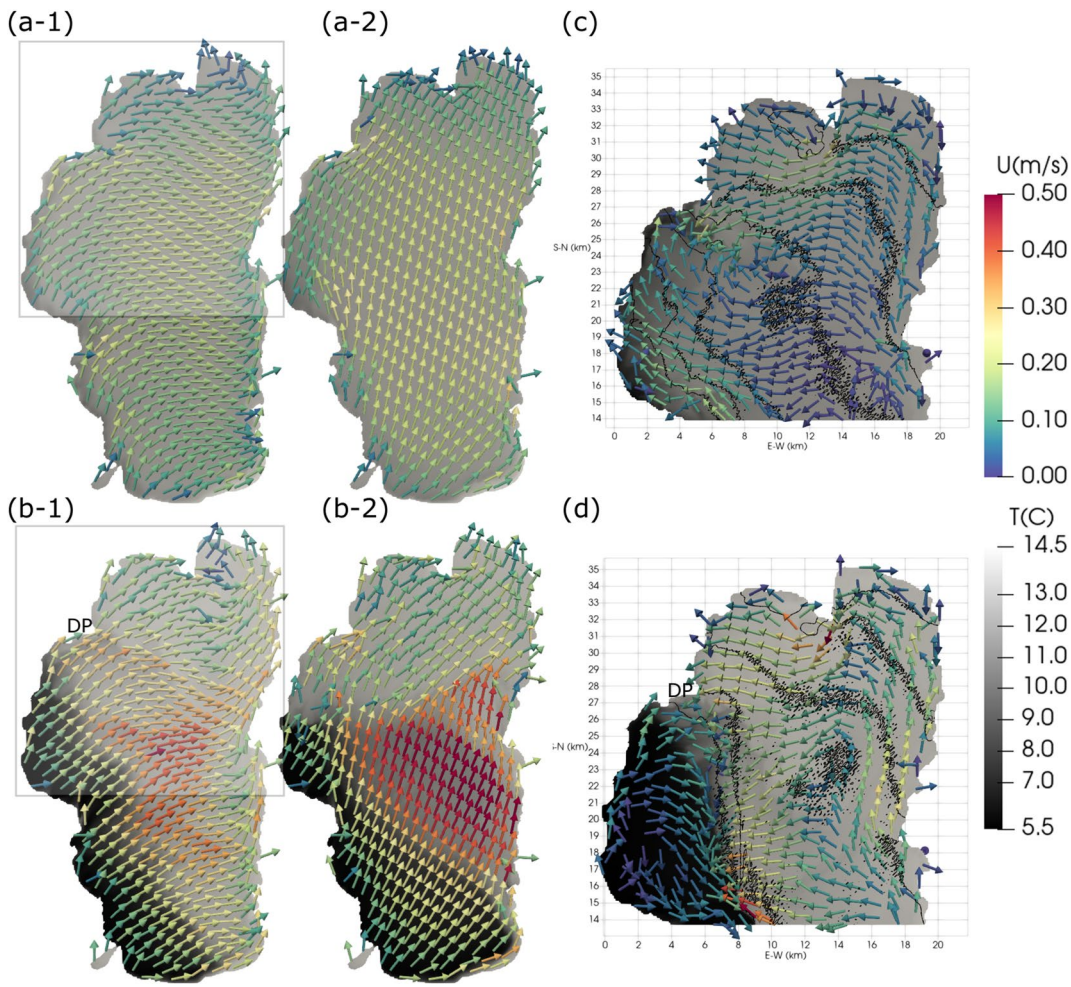

Figure 10. Coriolis force effect during upwelling setup (a), (b) and relaxation (c, d). (a, b) Rotational effects on thermal front shown by comparison between simulations with (x-1) and without Coriolis (x-2) force during E1 (a-x) and E3 (b–x). (c, d) are the zoomed view of square on (a) and (b) showing approximate geostrophic balance during upwelling relaxation E1 (c) and E3 (d) as indicated by quasi-parallel surface elevation isobars and surface velocity vectors.

In all upwelling events, Ekman transport in the surface layer was observed to play a significant role away from the coasts. Surface currents in simulations without Coriolis are consistently quasi-parallel to the wind direction and are only affected by the lake morphometry (Figures 10a and 10b). In contrast, numerical results that included the Earth's rotation showed Ekman transport in the pelagic zone (between 8 and 14 *km* from west shore). Nonetheless, wind-induced surface flows, near the shores, were approximately parallel to the wind direction in both cases. In particular, the simulations showed this behavior to be limited to about $2L_R$, ≈ 5 and 6.5 *km* for E1 and E3, respectively. This implies that the dynamics of the surface boundary layer near the shore resemble those predicted by the non-rotational conceptual model at all times during upwelling events. However, further offshore, where effective wind forcing time scales are longer, rotation is important and Ekman dynamics develop. The resulting flows cause divergence along coasts parallel to the wind direction, and generate surface cooling at shores to the left of the wind field in the northern hemisphere (i.e., coastal upwelling).

Furthermore, despite the similarity in the return flow structure between the simulations with and without Coriolis, the occurrence of quasi-geostrophic fronts was limited to the simulations that included the Coriolis force. Wind speeds during E1 caused an upwelling zone of ≈ 4 *km* similar to the internal Rossby radius of deformation $L_r = 2.5$ *km*, and thus rotational effects on the return flow (buoyant spreading) were limited. However, stronger winds in the third event created an upwelling zone that extended a distance from west shore $\geq 3L_r$ (i.e., ≈ 10 *km* for $L_r = 3$ *km*), allowing Coriolis effects to become as important as buoyancy effects during the relaxation. The resultant quasi-geostrophic frontogenesis slowed the westward propagation of the thermal front in E3, explaining the arrival of the coastal jet before the thermal front that propagates across the middle of the lake (Figure 5). In different lakes and under different wind forcing, these two modes of relaxation will interact in different ways with the shore-trapped jet flow reaching the upwelled shore more quickly in some circumstances (more rotational), and the propagation of the thermal front across the lake returning water faster in other cases (less rotational).

4.2. Coastal Jet: Rotational Lake Response

The jet-like flow structure, discussed in Section 3.2, possesses a maximum velocity which increased in time while winds prevailed. The jet structure was limited to the upper layer, similarly to previous observations in other rotationally influenced lakes (e.g., Csanady, 1972; Csanady & Scott, 1974), resembling the so-called coastal jet. While Kelvin waves as upwelling-driven response have been reported in lakes with similar or greater length scales as of Lake Tahoe (e.g., Rueda, 2003; Valipour et al., 2019; Vidal et al., 2013), the coastal jet signal has only been observed in large lakes as a response to wind stress.

Coastal jets are expected for estimations of the non-dimensional ratio $fBc^{-1} \geq 1$, which is only large enough in the baroclinic mode for common lake widths (Csanady, 1975). Following Gill (1982), for a two-layer flat bottom model, the internal wave phase speed, c, can be estimated as $c = \left(g\epsilon h_1 h_2 (h_1 h_2)^{-1}\right)^{1/2}$, where $\epsilon = (\rho_2 - \rho_1)\,\rho_2^{-1}$ with indices 1 and 2 referring to the epilimnion and the hypolimnion, respectively. Using the depth of the thermocline found for E1 and E3 in Section 3.1 (i.e., $h_1 = 12.2$ and 15 *m* for E1 and E3, respectively) and the mean epilimnion temperature during both upwellings $T_{E1} = 11.5°C$ and $T_{E3} = 12.9°C$, we obtain $c_{E1} = 0.2\ ms^{-1}$ and $c_{E3} = 0.28\ ms^{-1}$ as the internal wave phase speed accordingly.

Using $B = 20$ *km* as the lake flow length scale, $f = 9.18e^{-5}\ s^{-1}$ as the Coriolis frequency, and aforementioned c_{E1} and c_{E3} give estimations of the non-dimensional width channel of $fBc^{-1} = 8.5$ and $fBc^{-1} = 6.6$ for E1 and E3, respectively (Csanady, 1975). The results lead us to explore that coastal jets are expected in Lake Tahoe during the wind storms and stratification conditions present during the study period. Following the aperiodic solution in the baroclinic mode for coastal jets in a two-layer model with flat bottom and infinite straight coast by Csanady (1975) (i.e., Equation 2), gives estimates for the maximum theoretical coastal jet velocity. Integrating in time the northward component of the wind induced shear stress (wind parallel to the east shore) and using the estimated thicknesses for the epilimnion (h_1) and hypolimnion (h_2) during upwellings E1 and E3 result in maximum jet velocities of 0.40 ms^{-1} and 0.38 ms^{-1} for E1 and E3, respectively, on the east shore.

The dominant southwesterly winds during upwelling events promoted the formation of the coastal jets along the eastern shore of Lake Tahoe. These theoretical estimations are in good agreement with our model results during E3, where a maximum jet velocity 0.35 ms^{-1} was observed (Figure 7). Maximum jet velocity obtained from our model results are smaller compared to the theoretical estimation during E1. The difference found during E1 could be explained by the dissipation of energy and boundary mixing on the complex bathymetry, conditions

not considered in the theoretical model assumptions of infinite straight coast, straight walls, and flat bottom. Furthermore, difference during E1 is likely due to the decrease of the wind intensity in the middle of the event (Figure 4i). This relaxation of wind forcing allowed restoring forces to lessen the overall upwelling magnitude and thus the coastal jet maximum velocity.

The quantitative agreement for the maximum jet velocity between the theoretical and numerical results allow us to consider the flow structure of the coastal jet to be a rotational response. Furthermore, a balance between the barotropic pressures gradients and Coriolis force resulted in velocity vectors to be parallel to the barotropic pressure isobars (Figures 10c and 10d), implying that the coastal jet flow structure during upwelling is in approximate geostrophic balance. The coastal jet flow structure was bounded to the shore and its horizontal length scale was consistently of the order of the internal Rossby radius of deformation, similarly to coastal jets reported in large lakes (e.g., Csanady, 1972). The characteristics that describe the alongshore currents from our model results compare well to the theoretical approach for coastal jets and other studies in large lakes (e.g., Blanton, 1975; Csanady, 1975; Csanady & Scott, 1974; Valipour et al., 2019). Lastly, numerical simulations that considered null Coriolis force did not exhibit the coastal jet response during the relaxation stage (Figure S12 in Supporting Information S1).

The steep slopes and shallow shelf present at Crystal Bay and Agate Bay, respectively (Figure 1), promote the acceleration of the counterclockwise currents, generated on the east shore (Figure 7). Influenced by the shallow shelf on the northwestern region of the lake and a balance between the inertial forces and the Coriolis force, the coastal jet flows mainly toward the west shore rather than flowing along the coast and into Agate Bay. The main core of the coastal jet arrived to the northwestern shore (i.e., *DP* in Figures 1 and 10) before promoting the formation of a sub-basin clockwise rotational flow on the whole extent of Agate bay (Figures 5e–5h).

Favorable wind direction and lake morphometry allowed for the formation of the coastal jet. Characteristics of the alongshore currents such as: being trapped to widths that scale to L_r, being in quasi-geostrophic balance, and having maximum velocities comparable with the theoretical approach confirm that this aperiodic flow structure (coastal jet) is a purely rotational response to winds. In addition, for conditions such that $S < 0.3$, a combination of Kelvin and Poincaré waves are expected as lake response (Antenucci & Imberger, 2001; Stocker & Imberger, 2003). Cross-wavelet power in the Integrated Kinetic Energy (IKE) and Integrated Potential Energy (IPE) signals for the field data indicated the existence of periodic responses during the three upwelling events. In particular, a period of 128 *hr* was concluded to be consistent with a Kelvin wave excited during the upwelling events (Roberts et al., 2021). Estimates of the previously reported internal wave phase speed during E1 and E3 and average speed of the coastal jets, lead to consider that both, the aperiodic response (coastal jet) and cyclonic waves, combine into the flow structure observed at all upwellings (Figures 4–7; Csanady, 1975; Csanady & Scott, 1974).

4.3. Upwelling Dynamics

The expected strong rotational influence in the internal wavefield and the numerical results allow us to conclude that the response to prolonged wind events on rotationally influenced lakes with length scales similar to those of Lake Tahoe (i.e., 20 *km*) may be grouped into the following 3D flow structures. (1) The phenomenon initiates with upward flows on upwind coasts and shores to the left of the wind direction, and downward currents on the opposite shores, often represented by the tilting of the isotherms; (2) offshore surface currents non-parallel to the wind direction and affected by the Earth's rotation; (3) return flow of the thermal front due to baroclinic motions and affected by the Coriolis force; (4) cyclonic motions; (5) downward flow structure on upwelled shore post wind relaxation, internal wave breaking and shoaling; (6) coastal jet along the shore, forced by the wind parallel to the coastline, and dependent on the wind event duration. The resulting coastal jet flow structure is also affected by the lake morphometry (Figure 11).

It is to our knowledge that there is no clear threshold for the transition from one upwelling conceptual model to the other. As mentioned, upwelling setup dynamics have been described by applying the non-rotational framework and parameterization W in rotationally influenced lakes (e.g., Antenucci & Imberger, 2001; MacIntyre et al., 2009; Pöschke et al., 2015; Roberts et al., 2021). In these studies, upwelling timing and magnitude have been predicted correctly. Nonetheless, results from the numerical simulations imply that the lake response differs from the 2D response predicted by this model. The rotational nature of the observed flow structures indicates that

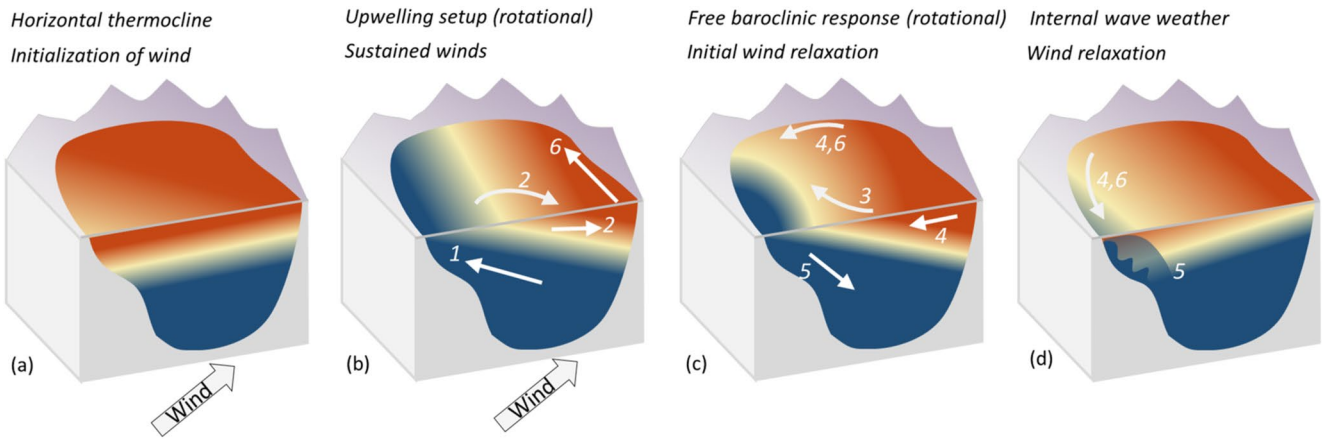

Figure 11. Upwelling setup and relaxation flow structures in rotationally influenced lakes. (a) Stratification before winds. (b) Rotational flow structures during upwelling setup. (c) Initialization of upwelling relaxation phase representing rotational flow response. (d) Passage of Kelvin waves and potential coastal jet with associated mixing and shoaling of internal wavefield. Adapted from Roberts et al. (2021).

the use of the 2D closed basin upwelling setup model, in lakes where $S \leq 1$, should be limited to predicting the timing of upwelling rather than interpreting the dynamics to be limited to the upwind boundary and constrained to the vertical plane; response often assumed when applying the W parameterization. The strong influence from the Earth's rotation in the flow structures during upwellings in these lakes exposes the need to establish the stratification and length scale limits for which the 2D closed-basin upwelling model satisfactorily describes the lake response to high-speed winds. Furthermore, it was found that water quality impacts during upwellings are not constrained to the upward fluxes at the upwind boundary. From this study it appears that rotation is less important during the short time scales of upwelling setup and more important during the longer time scales (much greater than $1/f$) of relaxation from upwelling.

4.4. Upwelling Water Quality Impacts

LPT analysis exhibited the mechanisms that can impact water quality in the nearshore during upwelling events in closed-basin rotationally influenced lakes. While the upward fluxes of constituents on the upwelled shore is one of the main mechanisms, a second important mechanism is the counterclockwise horizontal advection post wind relaxation.

The upward fluxes of nutrients and/or chl-a have been the focus of many limnology studies that address water quality impacts in lakes during upwellings (e.g., MacIntyre et al., 1999; Roberts et al., 2021). However, potential water quality impacts during upwelling relaxation due to rotational flow structures have received less attention. The strong horizontal currents generated during upwellings are sufficient to transport and disperse nutrients and plant fragments, and to resuspend fine sediments to areas of the lake typically less affected by localized watershed inflows. Trapped to the shore, within distances $\sim L_r$ from the shore, the coastal jet directly affects the littoral zone and potentially trap inflows, and thus nutrient loading, in the euphotic zone affecting the nearshore water quality (Rao & Schwab, 2007; see Figure 9). The numerical results showed the relevance of these transport processes during upwellings at other locations of the lake different from the upwelled zone, implying that water quality impacts during upwellings potentially alter the lake at multiple locations in a rotationally influenced lake.

5. Conclusions

Observed flow structures allow us to conclude that upwelling-driven dynamics in lakes of similar length scales, stratification conditions, and rotational influence to those of Lake Tahoe (e.g., Lake Tahoe with $S \approx 0.23$) are composed of 3D rotationally influenced phenomena. Nonetheless, as stated before, to-date the thresholds for separating the upwelling dynamics from rotational to non-rotational are not currently well established. Flow patterns from the numerical model during upwelling setup and relaxation phases are consistent with the rotational

influence predicted by the parameterization of the internal wavefield (S). During upwelling setup, surface cooling was observed both at the upwind boundary and to the left from the mean wind direction. Offshore currents were not restricted to the vertical plane or parallel to the wind direction, and described Ekman-driven flows. During wind forcing, surface flows near the shores were at all times non-rotational. However, at distances $\geq 2L_r$, the Coriolis force impacted the main flow, rotating the thermal front to the right of the mean wind direction. During the relaxation phase, the return flow of the surface layer developed a quasi-geostrophic front, implying the formation of flows parallel to the thermal front and a reduction in propagation of the front due to the strong influence of the Coriolis force.

Regarding the question "Can upwelling dynamics be described by a single conceptual model available in the literature?", posed in the introduction section, results obtained from our model reveal that upwelling dynamics in lakes with Burger numbers $S \leq 1$, and length scales $L \geq 20$ *km* can not be addressed by strictly following the non-rotational conceptual model as flow structures during upwelling setup and relaxation phases were 3D at all upwelling events. Given the data from the field deployment by Roberts et al. (2021), where instruments were located at about 2 *km* from the west shore, the upwelling setup was considered to be non-rotational (i.e., 2D) and only the relaxation phase was assumed to exhibit the effects of the Earth's rotation. The details of the lake response during upwellings from the numerical simulations revealed that the lake response to wind events is a superposition of both currently available conceptual models (i.e., non-rotational and coastal upwelling models). Therefore, future research must establish the limits for the combination of wind forcing, length scales, and stratification conditions for which the available upwelling setup conceptual models are valid and applicable to lake ecosystems.

Quasi-geostrophic balance describes the coastal jet signal that formed during wind forcing on the downwelled shore and that later flowed counterclockwise along the shore. Trapped to the shore and with widths that scale to L_r, these alongshore currents resemble quantitatively and qualitatively the coastal jets observed in rotationally influenced large lakes during wind events. The results allow us to conclude that the observed coastal jet flow structure is a purely rotational response, which may be accompanied by internal Kelvin waves.

Regarding the potential water quality impacts during upwellings in rotationally influenced lakes, the surface temperature patterns and LPT results allow us to conclude that water quality impacts during upwellings, in lakes different from the large lakes, are not limited to the upwind boundary but also upward fluxes of nutrients and chl-a can be expected at locations to the left of the wind direction. In addition, LPT results indicate that horizontal alongshore advection play a significant role in the water quality during upwellings and closed-basin effects should be investigated when addressing upwelling impacts in lakes generally considered to be rotational.

Data Availability Statement

Numerical simulation results can be reproduced using the Si3D executable file and input files in the public repository https://doi.org/10.5281/zenodo.5717466. The Zenodo public repository also provides the Si3D source code used and the time series numerical results for vertical profiles at multiple sites in the numerical domain. Output data of numerical results such as the 3D binary file is available from the corresponding author.

Acknowledgments
We would like to thank Drs. Stephen Monismith, Bernard Laval, and Galen Egan for their extensive contribution during the field deployment in 2018. We are also grateful to Brant Allen, Katie Senft, Brandon Berry, and Raph Townsend of the UC Davis Tahoe Environmental Research Center (TERC) for their invaluable field support during the field deployment and instrumentation. Simulations were undertaken in the UC Davis, College of Engineering, HPC2 supercomputer. The lake version of the Si3D code was developed by Dr. Francisco Rueda. Funding for this project was provided in part by the David and Dana Loury Foundation, and the UC Davis Tahoe Environmental Research Center.

References

Antenucci, J. P., & Imberger, J. (2001). Energetics of long internal gravity waves in large lakes. *Limnology and Oceanography*, *46*(7), 1760–1773. https://doi.org/10.4319/lo.2001.46.7.1760

Antenucci, J. P., Imberger, J., & Saggio, A. (2000). Seasonal evolution of the basin-scale internal wave field in a large stratified lake. *Limnology and Oceanography*, *45*(7), 1621–1638. https://doi.org/10.4319/lo.2000.45.7.1621

Blanton, J. O. (1975). Nearshore lake currents measured during upwelling and downwelling of the thermocline in Lake Ontario. *Journal of Physical Oceanography*, *5*(1), 111–124. https://doi.org/10.1175/1520-0485(1975)005<0111:nlcmdu>2.0.co;2

Corman, J. R., McIntyre, P. B., Kuboja, B., Mbemba, W., Fink, D., Wheeler, C. W., et al. (2010). Upwelling couples chemical and biological dynamics across the littoral and pelagic zones of Lake Tanganyika, East Africa. *Limnology and Oceanography*, *55*(1), 214–224. https://doi.org/10.4319/lo.2010.55.1.0214

Csanady, G. T. (1972). The Coastal Boundary Layer in Lake Ontario. Part I: The Spring Regime. *Journal of Physical Oceanography*, *2*(1), 41–53. https://doi.org/10.1175/1520-0485(1972)002<0041:tcblil>2.0.co;2

Csanady, G. T. (1975). Hydrodynamics of large lakes. *Journal of Fluid Mechanics*, *7*, 357–386. https://doi.org/10.1146/annurev.fl.07.010175.002041

Csanady, G. T. (1982). On the Structure of Transient Upwelling Events. *Journal of Physical Oceanography*, *12*(1), 84–96. https://doi.org/10.1175/1520-0485(1982)012<0084:otsotu>2.0.co;2

Csanady, G. T., & Scott, J. T. (1974). Baroclinic Coastal Jets in Lake Ontario during IFYGL. *Journal of Physical Oceanography*, *4*(4), 524–541. https://doi.org/10.1175/1520-0485(1974)004<0524:bcjilo>2.0.co;2

De la Fuente, A., Shimizu, K., Imberger, J., & Niño, Y. (2008). The evolution of internal waves in a rotating, stratified, circular basin and the influence of weakly nonlinear and nonhydrostatic accelerations. *Limnology and Oceanography*, *53*(6), 2738–2748. https://doi.org/10.4319/lo.2008.53.6.2738

Gill, A. E. (1982). *Atmosphere–Ocean Dynamics*. Academic Press, INC.

Hodges, B. R., Imberger, J., Saggio, A., & Winters, K. B. (2000). Modeling basin-scale internal waves in a stratified lake. *Limnology and Oceanography*, *45*(7), 1603–1620. https://doi.org/10.4319/lo.2000.45.7.1603

Horn, D. A., Imberger, J., & Ivey, G. N. (2001). The degeneration of large-scale interfacial gravity waves in lakes. *Journal of Fluid Mechanics*, *434*, 181–207. https://doi.org/10.1017/S0022112001003536

Hoyer, A. B., Schladow, S. G., & Rueda, F. J. (2015). A hydrodynamics-based approach to evaluating the risk of waterborne pathogens entering drinking water intakes in a large, stratified lake. *Water Resources*, *83*, 227–236. https://doi.org/10.1016/j.watres.2015.06.014

Imberger, J., & Patterson, J. C. (1990). *Physical Limnology* (Vol. 27). Academic Press, INC. https://doi.org/10.1016/S0065-2156(08)70199-6

Kantha, L. H., & Clayson, C. A. (1994). An improved mixed layer model for geophysical applications. *Journal of Geophysical Research*, *99*(C12), 25235. https://doi.org/10.1029/94JC02257

Kundu, P. K., Cohen, I. M., & Dowling, D. R. (2015). *Fluid Mechanics*. Elsevier Inc.

MacIntyre, S., Clark, J. F., Jellison, R., & Fram, J. P. (2009). Turbulent mixing induced by nonlinear internal waves in Mono Lake, California. *Limnology and Oceanography*, *54*(6), 2255–2272. https://doi.org/10.4319/lo.2009.54.6.2255

MacIntyre, S., Flynn, K. M., Jellison, R., & Romero, J. R. (1999). Boundary mixing and nutrient fluxes in Mono Lake, California. *Limnology and Oceanography*, *44*(3), 512–529. https://doi.org/10.4319/lo.1999.44.3.0512

MacIntyre, S., & Jellison, R. (2001). Nutrient fluxes from upwelling and enhanced turbulence at the top of the pycnocline in Mono Lake, California. *Hydrobiologia*, *466*, 13–29. https://doi.org/10.1023/A:1014563914112

MacIntyre, S., & Melack, J. M. (1995). Vertical and Horizontal Transport in Lakes: Linking Littoral, Benthic, and Pelagic Habitats. *Journal of the North American Benthological Society*, *14*(4), 599–615. https://doi.org/10.2307/1467544

Martin, J. L., & McCutcheon, S. C. (1999). In S. Wood (Ed.), (*Hydrodynamics and transport for water quality modeling*. *No. 1*) (Vol. 1). CRC Press. https://doi.org/10.1128/AAC.03728-14

Murphy, A. H., & Epstein, E. S. (1989). Skill Scores and Correlation Coefficients in Model Verification. *Monthly Weather Review*, *117*(3), 572–582. https://doi.org/10.1175/1520-0493(1989)117<0572:ssacci>2.0.co;2

Nakayama, K., Sato, T., Tani, K., Boegman, L., Fujita, I., & Shintani, T. (2020). Breaking of Internal Kelvin Waves Shoaling on a Slope. *Journal of Geophysical Research - C: Oceans*, *125*(10), 1–15. https://doi.org/10.1029/2020JC016120

Pöschke, F., Lewandowski, J., Engelhardt, C., Preuß, K., Oczipka, M., Ruhtz, T., & Kirillin, G. (2015). Upwelling of deep water during thermal stratification onset - A major mechanism of vertical transport in small temperate lakes in spring? *Water Resources Series*, *51*(12), 9612–9627. https://doi.org/10.1002/2015WR017579

Rao, Y. R., & Schwab, D. J. (2007). Transport and Mixing Between the Coastal and Offshore Waters in the Great Lakes: A Review. *Journal of Great Lakes Research*, *33*(1), 202–218. https://doi.org/10.3394/0380-1330(2007)33[202:tambtc]2.0.co;2

Reardon, K. E., Bombardelli, F. A., Moreno-Casas, P. A., Rueda, F. J., & Schladow, S. G. (2014). Wind-driven nearshore sediment resuspension in a deep lake during winter. *Water Resources Research*, *50*(11), 8826–8844. https://doi.org/10.1002/2014WR015396

Reiss, R. S., Lemmin, U., Cimatoribus, A. A., & Barry, D. A. (2020). Wintertime Coastal Upwelling in Lake Geneva: An Efficient Transport Process for Deepwater Renewal in a Large, Deep Lake. *Journal of Geophysical Research - C: Oceans*, *125*(8), 1–18. https://doi.org/10.1029/2020jc016095

Roberts, D. C., Egan, G. C., Forrest, A. L., Largier, J. L., Bombardelli, F. A., Laval, B. E., et al. (2021). The setup and relaxation of spring upwelling in a deep, rotationally influenced lake. *Limnology & Oceanography*, *66*(4), 1168–1189. https://doi.org/10.1002/lno.11673

Roberts, D. C., Moreno-Casas, P., Bombardelli, F. A., Hook, S. J., Hargreaves, B. R., & Schladow, S. G. (2019). Predicting Wave-Induced Sediment Resuspension at the Perimeter of Lakes Using a Steady-State Spectral Wave Model. *Water Resources Research*, *55*(2), 1279–1295. https://doi.org/10.1029/2018WR023742

Rueda, F. J., & Schladow, S. G. (2003). Dynamics of Large Polymictic Lake. II: Numerical Simulations. *Journal of Hydraulic Engineering*, *129*(2), 922–101. https://doi.org/10.1061/(asce)0733-9429(2003)129:2(92)

Rueda, F. J., Schladow, S. G., Monismith, S. G., & Stacey, M. T. (2005). On the effects of topography on wind and the generation of currents in a large multi-basin lake. *Hydrobiologia*, *532*(1), 139–151. https://doi.org/10.1007/s10750-004-9522-4

Rueda, F. J., Schladow, S. G., & Pálmarsson, S. Ó. (2003). Basin-scale internal wave dynamics during a winter cooling period in a large lake. *Journal of Geophysical Research*, *108*(C3), 3097. https://doi.org/10.1029/2001JC000942

Rueda, F. J., Vidal, J., & Schladow, G. (2009). Modeling the effect of size reduction on the stratification of a large wind-driven lake using an uncertainty-based approach. *Water Resources Research*, *45*(3), 1–15. https://doi.org/10.1029/2008WR006988

Scheu, K. R., Fong, D., Monismith, S. G., & Fringer, O. B. (2018). Modeling Sedimentation Dynamics of Sediment-Laden River Intrusions in a Rotationally-Influenced, Stratified Lake. *Water Resources Research*, *54*(6), 4084–4107. https://doi.org/10.1029/2017WR021533

Schladow, S. G., Pálmarsson, S. Ó., Steissberg, T. E., Hook, S. J., & Prata, F. E. (2004). An extraordinary upwelling event in a deep thermally stratified lake. *Geophysical Research Letters*, *31*(15). https://doi.org/10.1029/2004GL020392

Smith, P. (2006). *A semi-implicit, three-dimensional model for estuarine circulation* (Vol. 176). USGS Report.

Steissberg, T. E., Hook, S. J., & Schladow, S. G. (2005). Characterizing partial upwellings and surface circulation at Lake Tahoe, California-Nevada, USA with thermal infrared images. *Remote Sensing of Environment*, *99*(1-2), 2–15. https://doi.org/10.1016/j.rse.2005.06.011

Stocker, R., & Imberger, J. (2003). Energy Partitioning and Horizontal Dispersion in a Stratified Rotating Lake. *Journal of Physical Oceanography*, *33*(3), 512–529. https://doi.org/10.1175/1520-0485(2003)033<0512:epahdi>2.0.co;2

Swift, T. J., Perez-Losada, J., Schladow, S. G., Reuter, J. E., Jassby, A. D., & Goldman, C. R. (2006). Water clarity modeling in Lake Tahoe: Linking suspended matter characteristics to Secchi depth. *Aquatic Sciences*, *68*(1), 1–15. https://doi.org/10.1007/s00027-005-0798-x

Thompson, A., & Imberger, J. (1980). Response of a numerical model of a stratified lake to wind stress. In *2nd International Symposium on Stratified Flows* (pp. 562–570).

Valipour, R., Rao, Y. R., León, L. F., & Depew, D. (2019). Nearshore-offshore exchanges in multi-basin coastal waters: Observations and three-dimensional modeling in Lake Erie. *Journal of Great Lakes Research*, *45*(1), 50–60. https://doi.org/10.1016/j.jglr.2018.10.005

Vidal, J., MacIntyre, S., McPhee-Shaw, E. E., Shaw, W. J., & Monismith, S. G. (2013). Temporal and spatial variability of the internal wave field in a lake with complex morphometry. *Limnology & Oceanography*, *58*(5), 1557–1580. https://doi.org/10.4319/lo.2013.58.5.1557

References From the Supporting Information

Huang, W., & Malcolm, S. (1995). Discussion: 3D Model of Estuarine Circulation and Water Quality Induced by Surface Discharges. *Journal of Hydraulic Engineering*, *121*(4), 300–311. https://doi.org/10.1061/(asce)0733-9429(1995)121:4(300)

Ramón, C., Cortés, A., & Rueda, F. J. (2015). Inflow–outflow boundary conditions along arbitrary directions in Cartesian lake models. *Computers & Geosciences*, *74*, 87–96. https://doi.org/10.1016/j.cageo.2014.10.002

Rueda, F. J. (2001). *A three-dimensional hydrodynamic and transport model for lake environments (Unpublished doctoral dissertation)*. University of California Davis.

Rueda, F. J., & MacIntyre, S. (2009). Flow paths and spatial heterogeneity of stream inflows in a small multibasin lake. *Limnology & Oceanography*, *54*(6), 2041–2057. https://doi.org/10.4319/lo.2009.54.6.2041